

\mathcal{J} -Invariant Volume Shuffle for Self-Supervised Cryo-Electron Tomogram Denoising on Single Noisy Volume

Xiwei Liu¹ Mohamad Kassab¹ Min Xu² Qirong Ho¹

¹Mohamed bin Zayed University of Artificial Intelligence ²Carnegie Mellon University

{Xiwei.Liu, Mohamad.Kassab, Qirong.Ho}@mbzuai.ac.ae mxul@cs.cmu.edu

Abstract

Cryo-Electron Tomography (Cryo-ET) enables detailed 3D visualization of cellular structures in near-native states but suffers from low signal-to-noise ratio due to imaging constraints. Traditional denoising methods and supervised learning approaches often struggle with complex noise patterns and the lack of paired datasets. Self-supervised methods, which utilize noisy input itself as a target, have been studied; however, existing Cryo-ET self-supervised denoising methods face significant challenges due to losing information during training and the learned incomplete noise patterns. In this paper, we propose a novel self-supervised learning model that denoises Cryo-ET volumetric images using a single noisy volume. Our method features a U-shape \mathcal{J} -invariant blind spot network with sparse centrally masked convolutions, dilated channel attention blocks, and volume-unshuffle/shuffle technique. The volume-unshuffle/shuffle technique expands receptive fields and utilizes multi-scale representations, significantly improving noise reduction and structural preservation. Experimental results demonstrate that our approach achieves superior performance compared to existing methods, advancing Cryo-ET data processing for structural biology research. Code is available at <https://github.com/Xiwei-web/SelfCryoET>.

1. Introduction

Cryo-Electron Tomography (Cryo-ET) is an advanced imaging technique that provides the visualization of cellular structures and macromolecular complexes in three dimensions at near-native states [37]. Combining the principles of Cryo-Electron Microscopy (cryo-EM) with tomographic reconstruction [14], Cryo-ET creates detailed 3D images of specimens that have been rapidly frozen, preserving their natural structure without the need for staining or chemical fixation. However, Cryo-ET images typically suffer from a low signal-to-noise ratio (SNR). Several factors contribute to this issue: low electron doses to prevent radiation damage result in weaker signals [1], the thickness of biological spec-

imens causes electron scattering, and the cryogenic conditions introduce additional noise. Consequently, the high levels of noise can obscure fine structural details, complicate the tomographic reconstruction process, and make data interpretation challenging [5].

Traditional denoising methods [6], [13], [36], [32] often fall short in handling the complex noise patterns inherent in Cryo-ET data. These methods rely on predefined assumptions about the noise and signal characteristics, limiting their flexibility and performance. In recent years, deep neural networks (DNNs) have emerged as powerful tools for image denoising [19], [40], [48]. Supervised learning approaches, which rely on large datasets of paired noisy and clean images, have shown promise. However, acquiring paired datasets for Cryo-ET is extremely challenging due to the difficulty in obtaining high-quality ground truth data.

To address the abovementioned challenges, self-supervised denoising methods have gained attention. Unlike supervised methods, the model in self-supervised learning, which uses the same image for both input and target, has to satisfy \mathcal{J} -invariance [4]. \mathcal{J} -invariance ensures that the prediction for each pixel is not influenced by its original value. Blind-spot networks (BSNs) [22], which satisfy the \mathcal{J} -invariance requirement, have been successfully implemented for denoising noisy inputs in a self-supervised manner [24] [46]. As summarized in Table 1, SC-Net [42] adapts a volumetric blind-spot strategy on input volume to maintain \mathcal{J} -invariance. Nevertheless, SC-Net only uses masked volumetric patches for model training, which can lead to resource wastage and loss of information during training. Both SC-Net and NMSG [16] utilize U-Net as their primary architecture, while NMSG has to utilize Generative Adversarial Networks (GANs) [16] to learn and model the noise patterns present in Cryo-ET data, generating pairs of noisier and noisy images for training. By constructing a BSN with centrally masked convolutions (CMC) and dilated convolution layers (DCL), we can address these limitations without the need for GANs to pre-learn Cryo-ET noisy patterns. Additionally, the centrally masked convolutions in BSN ensure that all voxels participate in train-

Table 1. Comparison of the exiting self-supervised denoising methods for Cryo-ET

Feature	Ours	SC-Net	NMSG	Noise2Void
Main Architecture	U-shape \mathcal{J}-invariant BSN	Tradition U-Net	Tradition U-Net	Tradition U-Net
Key Components	CMC+DCA+VU/S	Conv3D+BN3D+LReLU	Conv3D+BN3D+LReLU	Conv3D+BN3D+LReLU
\mathcal{J} -invariance	Meet	Meet (information loss)	Doesn't Meet	Meet
downsampling/upsampling	volume-unshuffle/shuffle	max pooling / interpolation	max pooling / interpolation	max pooling / interpolation

ing [47], unlike the mask-in-input strategy of SC-Net that leads to information loss. However, most current methods use BSN built with stacked CMC and DCLs instead of U-shape network [39], [24], [46], as traditional downsampling operation breaks \mathcal{J} -invariance.

As we know that U-Net structures are particularly effective in capturing long-range dependencies and coarse-to-fine representations [10], [43], [45]. To keep leveraging U-Net in self-supervised learning, we propose volume-unshuffle/shuffle (VU/S), a suitable downsampling/upsampling technique for volumetric images that preserves \mathcal{J} -invariance. We incorporated sparse centrally masked convolutions, dilated channel attention (DCA) block [9] and volume-unshuffle/shuffle to build a novel \mathcal{J} -invariant U-shape self-supervised learning model, specifically designed for denoising Cryo-ET volumetric images using a single noisy volume. Our method is validated through extensive experiments on both simulated and real-world Cryo-ET datasets. The results demonstrate that our approach outperforms existing self-supervised denoising methods based on single noisy volumes, achieving superior noise reduction and structural preservation.

Our contribution can be summarized as follows:

- A novel U-shape self-supervised volumetric image denoising model is introduced, by adapting sparse centrally masked convolution and dilated channel attention (DCA) blocks to build a \mathcal{J} -invariant blind spot network.
- We propose a novel downsampling/upsampling technique called volume-unshuffle/shuffle, which preserves the \mathcal{J} -invariance property essential for effective denoising. This technique expands the receptive fields and utilizes multi-scale representation, significantly improving the model's ability to capture long-range dependencies and structural details within the Cryo-ET volumetric data.
- We introduce dilated channel attention (DCA) block to the domain of Cryo-ET volumetric images denoising, which effectively incorporate global context through channel attention.
- We design a combined loss function that balances noise suppression with structure preservation. This includes structural reconstruction loss, contrast guidance loss, edge enhancement loss, and total variation loss, ensuring that the denoised output retains essential structural details.

2. Related Works

Traditional volumetric image denoising. Cryo-ET data processing traditionally involves denoising either before or after tomographic reconstruction. Methods that denoise projections before reconstruction [27] often fail to maintain the 2D-to-3D relationship defined by the Fourier-slice theorem [33], resulting in overly smoothed volumes. Linear filters such as low-pass filters, Gaussian filters, and dose filtering are easy to adapt and tune but often lack the sophistication needed for complex noise patterns. Nonlinear filters include the iterative median filter [38], nonlinear anisotropic diffusion (NAD) [13], bilateral and trilateral filters [36], Non-local Means (NLM) [6], and BM4D (Block-Matching and 4D Filtering) [26]. These traditional methods often rely on predefined assumptions about the data, limiting their flexibility and performance in varying scenarios.

Supervised learning image restoration. DNNs have shown great promise in image denoising. Supervised learning approaches, which rely on large datasets of paired noisy and clean images, have demonstrated significant advancements. Jain et al. [19] first employed DNN for image denoising, achieving results comparable to the best traditional algorithms at the time. Subsequently, more DNN-based methods were proposed [48] [49], [40], [12], [2]. Encoder-Decoder networks [28] and GANs [18] have also been used for image restoration. However, acquiring high-quality paired datasets for Cryo-ET is extremely challenging, limiting the application of supervised learning methods in this field.

Self-supervised learning image restoration. Self-supervised denoising methods do not require paired noisy and clean datasets, making them particularly suitable for Cryo-ET data. Noise2Noise (N2N) [25] was the first self-supervised algorithm that achieved performance comparable to supervised image denoising by training on only aligned noisy-noisy image pairs. Topaz-Denoiser [5] and CryoCARE [7], based on the N2N concept, have been effectively applied to Cryo-EM and Cryo-ET. These approaches train a neural network using pairs of noisy images to distinguish between signal and noise without needing clean reference images. However, acquiring a large number of noisy volumes of the same sample can be impractical and time-consuming, limiting the availability of training data. Noisier2Noise [31] extended this concept by adding synthetic noise to noisy images to create training pairs. The NMSG [41] method leverages GANs to pre-learn the noise

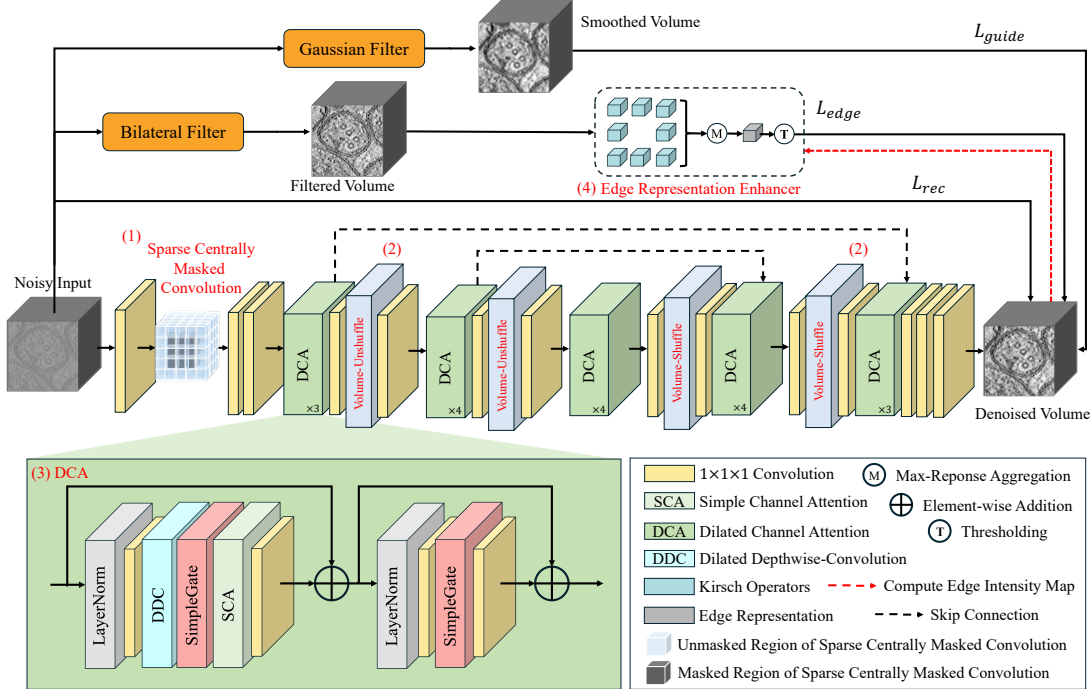


Figure 1. The architecture of proposed method. The noisy input volume is first preprocessed using (i) 3D Gaussian filters to generate a smoothed volume and (ii) bilateral filters to create a edge preserved filtered volume, respectively. We construct the U-shape BSN with 4 main contributions: (1) Sparse centrally masked convolution, (2) Volume Unshuffle/Shuffle and (3) DCA blocks, with (4) an edge representation enhancer utilizes the filtered volume to guide model training. Refer to Section 4.2 for details.

pattern in tomogram, generating pairs of noisier and noisy images for training. However, NMSG extracts several 2D noise slices only from the top and bottom slices in the raw noisy volume as the learning targets for noise modeling. This approach may not capture the full variability and intricacies of the noise present throughout the entire 3D volume, due to the inherent complexity and heterogeneity of noise patterns in Cryo-ET data. Derived from Noise2Void [22], SC-Net [42] proposed a volumetric blind-spot replacement strategy, designed for Cryo-ET, extending the blind-spot concept into three dimensions. However, only the masked volumetric patches participate in model training each time, leading to wasted resources and time. Additionally, the masked volumetric patches no longer appear in the training process, resulting in the loss of information during training.

As the most widely used self-supervised denoising method, BSN was firstly proposed in Noise2Void, which is a special CNN that masks pixel in the center of the receptive field, and uses the surrounding information to reconstruct the information of the masked pixels. Variations like Laine19 [23], D-BSN [39], AP-BSN [24], MM-BSN [46] and PUCA [20] have prove their effectiveness of learning and removing the complicated noise pattern. These advancements highlight the promising future to refine self-supervised denoising techniques for Cryo-ET, addressing the unique challenges posed by the complex noise patterns and the lack of paired datasets.

3. Preliminaries

Following the assumption proposed in the work by Yang [42], we assume that a projection image $I_n(x, y)$ in cryo-ET represents a discrete observation of the projection $P_n(x, y)$ with additive Gaussian noise $N(x, y)$. This can be expressed as $I_n = P_n + N_n$. Therefore, we have:

Lemma 1 *The additive Gaussian noise in 2D projection remains Gaussian noise in the 3D reconstruction.*

$$V(x) = \Psi(x) + N(x), \quad (1)$$

where $V(x)$ represents the volumetric image reconstructed from a series of I_n , $\Psi(x)$ is the ideally noise-free image reconstructed from P_n , and $N(x)$ is the noise in the 3D space. This assumption provides the theoretical foundation for our method, ensuring that the noise characteristics are consistent during the transition from 2D to 3D.

\mathcal{J} -invariance is a critical concept in self-supervised image denoising, aimed at preventing models from learning to replicate noisy inputs directly. Noise2Self [4] firstly point out that the self-supervised denoising function f should be \mathcal{J} -invariant, the definition is as follows.

Definition 1 *Consider a partition \mathcal{J} of the dimensions $\{1, \dots, m\}$, and select J as a subset from \mathcal{J} . A function $f : \mathbb{R}^m \rightarrow \mathbb{R}^m$ is defined as \mathcal{J} -invariant if, for any given partition J , the output $f(x)_{,J}$ is entirely independent of the*

input values x_J within that subset. In other words, f maintains \mathcal{J} -invariance if $f(x)_J$ remains constant regardless of changes in x_J , where $f(x)_J$ and x_J denote the values of $f(x)$ and x restricted to J , respectively. This ensures that the prediction for each pixel relies solely on the surrounding pixel values, not on the pixel itself.

4. Methodology

4.1. Network Architecture

The proposed model begins with the raw noisy volumetric Cryo-ET data as shown in Figure 1. Initially, the data undergoes preprocessing using Gaussian and bilateral filters to generate smoothed and edge-preserved filtered volumes, respectively. These volumes are then divided into smaller overlapping patches. The patches are fed into a 2-level U-shape encoder-decoder network [35] designed for volumetric image denoising.

The encoding path starts with a $5 \times 5 \times 5$ sparse centrally masked convolution layer, which ensures \mathcal{J} -invariance by preventing the output voxels from being influenced by their corresponding input voxels. This layer is followed by volume-unshuffle operations at each level to downsample the input, effectively increasing the channel dimensions while reducing the spatial dimensions, capturing multi-scale features and expanding the receptive fields. Within the encoder, features are processed by DCA blocks. These blocks with the channel attention mechanisms integrate global context, enhancing the network’s ability to distinguish between noise and meaningful features.

The decoding path restores the spatial resolution using volume-shuffle operations, which reverse the downsampling process of volume-unshuffle. Skip connections are used to merge features from corresponding encoder levels, ensuring that detailed structures and textures are retained in the restored images. The final output image is generated by sequentially applying $1 \times 1 \times 1$ convolution layers to the merged features, resulting in a denoised image.

4.2. Main Components

(1) Sparse Centrally Masked Convolution. In Cryo-ET data, the complexity of three-dimensional structures and significant noise levels necessitate a robust approach for effective denoising. Traditional centrally masked convolutions, which mask only the central pixel, are inadequate for this task. Instead, we employ a sparse centrally masked convolution, using a $5 \times 5 \times 5$ kernel with the central $3 \times 3 \times 3$ region entirely masked. This design offers several advantages. First, the larger receptive field captures broader contextual information, crucial for understanding volumetric data and differentiating between signal and noise. Second, by masking a larger central region, we ensure \mathcal{J} -invariance, preventing the model from learning identity mappings and

enhancing its generalization to unseen noisy data. Third, the method adapts to the strong coherent ultrastructures in Cryo-ET data, balancing noise reduction and structure preservation. This approach focuses on the surrounding context, minimizing the influence of noise and preserving fine structural details, ultimately improving denoising performance.

(2) Volume Unshuffle/Shuffle. Inspired by [20], we propose a volume unshuffle/shuffle technique that significantly increases the receptive fields of the neural network, thereby enhancing its ability to capture long-range dependencies and multi-scale context within volumetric images. Downsampling, achieved through this technique, helps the denoiser understand the relationships and dependencies between different parts of the volume more effectively. In 2D image processing, pixel-unshuffle/shuffle methods that preserve original pixels have proven to be effective in image restoration. However, directly applying pixel-unshuffle to 3D volumetric images with voxels disrupts the \mathcal{J} -invariance property of BSN, which is essential for preventing the network from learning identity mappings (shown in supplementary material S1).

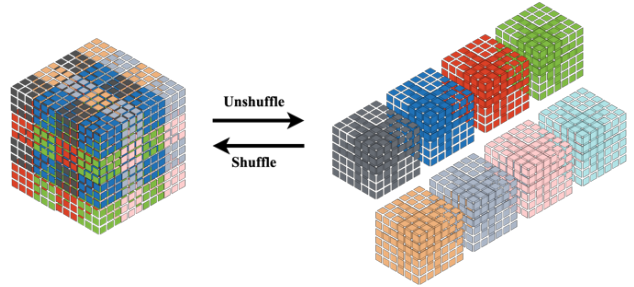


Figure 2. Volume unshuffle and shuffle.

To address this issue, we introduce the volume-unshuffle technique for volumetric tomogram images. Volume-unshuffle transforms a tensor of size $D \times H \times W \times C$ into a reshaped tensor of size $\frac{D}{v} \times \frac{H}{v} \times \frac{W}{v} \times (C \cdot v^3)$, where v represents the shuffle volume size, as illustrated in Figure 2. This transformation process ensures that the spatial information is redistributed into the channel dimension, thereby preserving the spatial structure while expanding the receptive field. This process can be mathematically defined as follows:

$$\text{Volume-Unshuffle}(y_{i,j,k,m}^{(l)}, v) = y_{i',j',k',m'}^{(l)} \quad (2)$$

$$i' = v \left\lfloor \frac{i}{v^3} \right\rfloor + (i \bmod v) \quad (3)$$

$$j' = v \left\lfloor \frac{j}{v^3} \right\rfloor + (j \bmod v) \quad (4)$$

$$k' = v \left\lfloor \frac{k}{v^3} \right\rfloor + (k \bmod v) \quad (5)$$

$$m' = C\left(v \left[\frac{i \bmod v^3}{v} \right] + \left[\frac{j \bmod v^3}{v} \right] + \left[\frac{k \bmod v^3}{v} \right]\right) + m \quad (6)$$

As demonstrated in Supplementary Material S2, our networks ensure the preservation of \mathcal{J} -invariance by employing volume-unshuffle with a volume size $v = 3$ equals to dilation factor $d = 3$. This integration of volume-unshuffle in BSN allows for effective downsampling operations while maintaining the independence of each voxel’s prediction from its input value. Moreover, the volume-shuffle operation, which acts as the reverse process of volume-unshuffle, facilitates the upsampling of downsampled feature maps, restoring them to their original volume sizes. This operation ensures that detailed structural information is preserved during the denoising process, leading to superior performance in noise reduction and ultrastructure maintenance.

(3) Dilated Channel Attention (DCA). The DCA blocks in the proposed network work in conjunction with the sparse centrally masked convolution at the beginning of the network to form the BSN. To fulfill the blind-spot characteristic, we incorporate a 3-dilated $3 \times 3 \times 3$ depth-wise convolution (DDC) before the gating and attention mechanisms. This follows D-BSN [39], which uses a centrally masked convolution kernel size of $k = 2d - 1$. The DCA blocks leverage this structure to incorporate global context via attention mechanisms, enhancing the denoising process by focusing on relevant features and suppressing noise.

The DCA block consists of several components: LayerNorm [3], a $1 \times 1 \times 1$ convolution, skip connection, SimpleGate [17], and Simplified Channel Attention (SCA) [9], along with DDC. LayerNorm is used to normalize the input features, ensuring stable training. The $1 \times 1 \times 1$ convolution helps in reducing the dimensionality and computational complexity. The skip connection facilitates the flow of information, preserving essential features across different layers. The utilization of SimpleGate and SCA enhances the integration of local and global information by suppressing less informative features [44].

(4) Edge Representation Enhancer. The edge and texture information captured in the bilateral filtered volume provides complementary guidance for tomographic restoration. As shown in Figure 3, this edge representation enhancer excels in extracting detailed edge and contour information by leveraging multi-directional edge detection. This representation significantly aids the training process when integrated into the network. More details are in Supplementary Material S6.

4.3. Loss Function

A combined loss function is introduced to our model for both noise removal and structure preservation.

Structural reconstruction loss. The structural reconstruction loss ensures the denoised output retains the essential details of the original noisy input. Formulated for

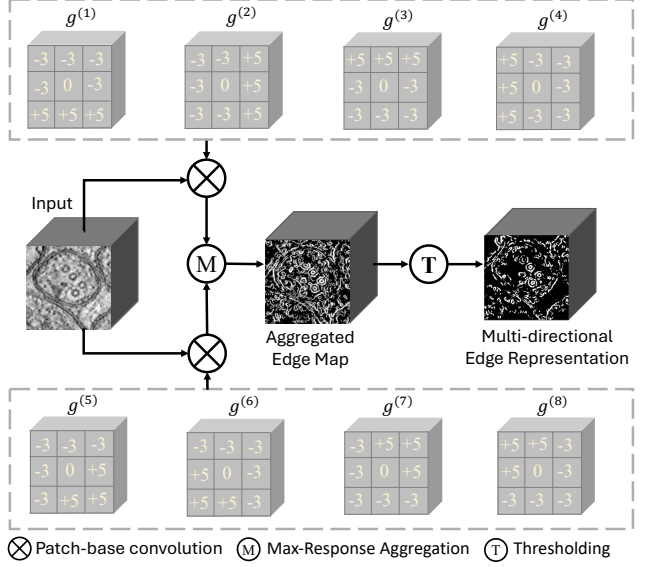


Figure 3. Details of edge representation enhancer.

a BSN, this loss function is defined as:

$$\mathcal{L}_{\text{rec}} = \mathbb{E} \left[\|f_{\theta}(V_i(x)) - V_i(x)\|_2^2 \right] \quad (7)$$

where f_{θ} is the denoising network parameterized by θ , and $V_i(x)$ represents the i -th raw noisy input volumetric patch. By minimizing this loss, the network effectively filters out noise and maintains the integrity of the underlying structures, leading to higher-quality reconstructions and better downstream analysis.

Contrast guidance loss. The contrast guidance loss aims to balance noise suppression and the preservation of ultrastructural details. To achieve this, a 3D Gaussian filter is applied to the raw noisy volume, producing a smoothed volume $V_f(x)$ that capturing mid- and low-frequency contrast information in order to recover the ultrastructure with higher contrast in the situation of training without ground truth. The loss function is defined as:

$$\mathcal{L}_{\text{guide}} = \mathbb{E} \left[\|f_{\theta}(V_i(x)) - V_{if}(x)\|_2^2 \right] \quad (8)$$

where $V_{if}(x)$ is the i -th filtered volumetric patch.

Edge enhancement loss. Bilateral filtering can smooth the image while preserving edge information, whereas gaussian filtering tends to blur the edges. Since bilateral filtering takes into account both spatial and intensity domains, it assigns smaller weights to pixels with significant intensity differences, thereby reducing noise while preserving more edges and details. We adapt edge enhancement extractor K on network output $f_{\theta}(V_i(x))$ and bilateral filtering reference volume $V_{ib}(x)$ to extract the intensity maps. Thus the edge enhancement loss can be defined as:

$$\mathcal{L}_{\text{edge}} = \mathbb{E} \left[\|K(f_{\theta}(V_i(x))) - K(V_{ib}(x))\|_2^2 \right] \quad (9)$$

This loss complements the contrast guidance loss by preserving of edges and details that might be lacking.

Table 2. Quantitative comparison on simulated datasets. (Metrics: PSNR(db)/SSIM). The **best** results among methods that do not require ground truth are highlighted, and the tilde (~) indicates approximate running time.

Methods	Shrec2020			Shrec2021			PolNet		Running time (mins)	
	0.1	0.15	0.2	0.1	0.15	0.2	0.1	0.2		
Noisy	24.14 / 0.598	20.63 / 0.440	18.12 / 0.377	24.36 / 0.252	20.84 / 0.179	18.34 / 0.142	27.19 / 0.601	23.67 / 0.448	21.17 / 0.344	
Non-learning	Gaussian	28.96 / 0.785	23.49 / 0.533	20.05 / 0.469	27.88 / 0.331	24.62 / 0.214	21.22 / 0.186	30.07 / 0.693	26.81 / 0.515	24.37 / 0.379
	Bilateral	26.89 / 0.707	22.37 / 0.461	18.11 / 0.372	27.79 / 0.324	22.02 / 0.191	18.91 / 0.167	29.82 / 0.643	25.35 / 0.478	24.65 / 0.381
	LPF	26.34 / 0.673	21.41 / 0.449	18.96 / 0.386	26.15 / 0.285	22.74 / 0.198	19.19 / 0.153	27.56 / 0.610	24.14 / 0.453	21.49 / 0.352
	NAD	27.77 / 0.736	24.49 / 0.564	21.31 / 0.492	28.13 / 0.357	25.92 / 0.222	20.74 / 0.177	29.91 / 0.687	25.48 / 0.503	22.27 / 0.369
	NLM	24.96 / 0.612	20.34 / 0.437	17.79 / 0.351	25.09 / 0.267	21.12 / 0.188	17.98 / 0.137	27.82 / 0.613	22.75 / 0.424	21.83 / 0.351
	BM4D	30.11 / 0.868	29.33 / 0.862	29.73 / 0.877	34.77 / 0.817	32.59 / 0.779	31.81 / 0.736	35.26 / 0.893	33.36 / 0.849	31.54 / 0.814
Supervised	DnCNN	39.67 / 0.966	39.57 / 0.959	38.92 / 0.954	42.77 / 0.944	42.54 / 0.947	41.85 / 0.938	42.36 / 0.985	42.53 / 0.979	40.82 / 0.971
	FFDNet	41.53 / 0.971	41.51 / 0.976	40.89 / 0.963	43.06 / 0.952	42.19 / 0.942	42.26 / 0.931	42.73 / 0.981	41.77 / 0.968	41.13 / 0.961
	V-Net	40.82 / 0.967	40.14 / 0.966	39.92 / 0.952	42.81 / 0.961	41.11 / 0.957	40.95 / 0.946	42.48 / 0.987	40.54 / 0.972	40.89 / 0.953
Self-supervised	N2V	24.38 / 0.602	20.19 / 0.428	17.55 / 0.363	24.13 / 0.241	20.69 / 0.168	18.29 / 0.143	26.54 / 0.592	22.93 / 0.426	21.21 / 0.341
	SC-Net	31.22 / 0.921	30.01 / 0.903	28.44 / 0.878	33.96 / 0.796	30.15 / 0.771	29.78 / 0.704	32.73 / 0.927	30.51 / 0.895	27.62 / 0.852
	NMSG	36.10 / 0.944	34.83 / 0.923	34.91 / 0.915	36.47 / 0.812	35.56 / 0.809	35.17 / 0.766	38.28 / 0.975	36.44 / 0.929	34.07 / 0.893
	Ours	36.02 / 0.941	36.18 / 0.952	35.79 / 0.936	39.23 / 0.832	38.16 / 0.810	37.64 / 0.784	38.90 / 0.966	37.06 / 0.953	36.51 / 0.932

Total variation loss. Total variation loss (TV Loss) is a regularization method commonly used in image denoising and image reconstruction. It works by minimizing the total variation of the image gradient, which smooths local regions without over-blurring edges. The TV loss for a volumetric image is defined as:

$$\mathcal{L}_{TV} = \sum_{r,s,t} (|\nabla_x V(r,s,t)| + |\nabla_y V(r,s,t)| + |\nabla_z V(r,s,t)|) \quad (10)$$

where $V(r,s,t)$ represents the voxel value at position (r,s,t) in the network output $f_\theta(V_i(x))$. $\nabla_x, \nabla_y, \nabla_z$ represent the gradients in the $x, y,$ and z directions, respectively. By penalizing large gradients, TV loss maintains the structural integrity of the image while reducing noise.

Eq. 7, 8, 9, 10 are combined to formulated the complete loss function of the denoising network:

$$\mathcal{L}_{total} = \lambda_1 \mathcal{L}_{rec} + \lambda_2 \mathcal{L}_{guide} + \lambda_3 \mathcal{L}_{edge} + \lambda_4 \mathcal{L}_{TV} \quad (11)$$

where $\lambda_1, \lambda_2, \lambda_3$ and λ_4 are the weight parameters of the loss functions.

5. Experiments

We evaluated the performance of our method on three simulated datasets and four real Cryo-ET datasets, The proposed model is compared with single volume-based methods including non-learning methods Gaussian filter, Bilateral filter [36], Low-pass filter (LPF), NAD [13], NLM filter [6], BM4D [26]. We also compare it with supervised method like DnCNN [48], FFDNet [49], and V-Net [30], and self supervised learning based method like Noise2Void (N2V) [22], SC-Net [42] and NMSG [41], resulting in a detailed quantitative empirical analysis. The sources of datasets can be found in Supplementary Material S3.

5.1. Networks Training Details

Our method is implemented by Pytorch [34] with the model was trained on one NVIDIA GeForce RTX 4090 GPU for all the experiments. The model is trained with single noisy volume each time. During the training, the batch

size was set to 2 with 108^3 patch size and 20% of the patches are selected as validation. The model was trained by 15 epochs for each noisy data, where the optimizer is Adam [11] with $\beta_1 = 0.5$ and $\beta_2 = 0.999$. The learning rate was set to 0.0002. For Eq. 11, the parameters were set as $\lambda_1 = 0.8, \lambda_2 = 0.5, \lambda_3 = 0.05$ and $\lambda_4 = 0.01$.

5.2. Experiments on Simulated Data

To assess the performance of our proposed method, we conducted experiments on three simulated datasets: SHREC2020, SHREC2021, and a private dataset obtained using the simulation software PolNet [29]. These datasets were generated with varying levels of additive white Gaussian noise (AWGN) at intensities $\sigma = 0.1, 0.15$ and 0.2 , following the procedure outlined in [42].

The PSNR and SSIM values in Table 6 demonstrate the robustness of our method in maintaining structural integrity while effectively reducing noise. Supervised methods in Table 6 tend to have faster running times, but their dependence on clean data limits their real-world applicability in Cryo-ET. Despite the inherent limitation of not using pixel information directly and slightly slower, our method demonstrates superior performance among self-supervised approaches, offering a balanced trade-off between denoising quality and applicability in scenarios without paired datasets. Visual comparison can be found in Supplementary Material S7.

Table 3. Quantitative results for different missing wedge levels. (AWGN: $\sigma=0.2$, metrics: PSNR(db)/SSIM)

Angular Range	MW Level	Noisy	Denoised
-70.0° to +70.0° (step 2°)	Moderate	23.72 / 0.496	38.53 / 0.948
-60.0° to +60.0° (step 2°)	Standard	21.59 / 0.371	36.48 / 0.934
-40.0° to +40.0° (step 2°)	Severe	16.81 / 0.304	35.49 / 0.906
-30.0° to +30.0° (step 2°)	Extreme	12.63 / 0.234	31.92 / 0.822

To assess the missing wedge (MW) effect [15] on our model, we generated simulated tomograms with varying MW levels by adjusting the tilt series angular range. As shown in Table 3, despite performance decreases with more

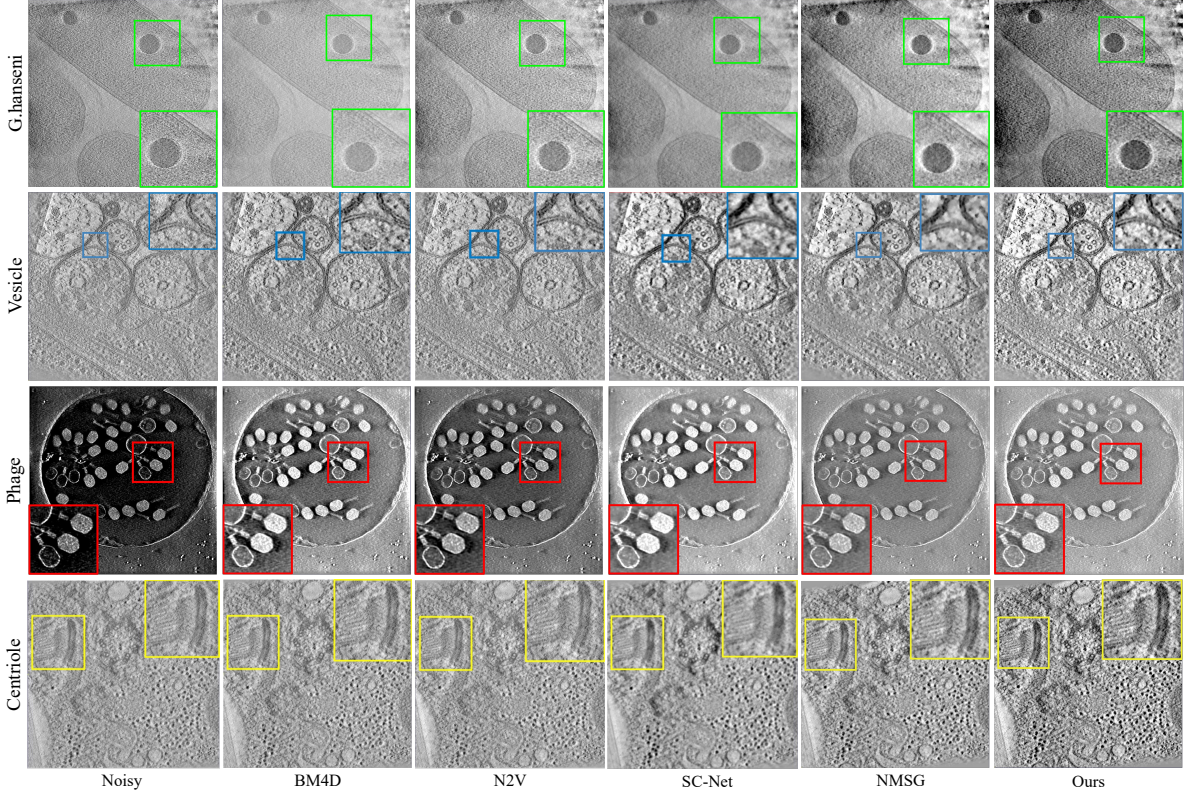


Figure 4. Visual results of the real data.

severe MW, the model still preserves structure well, demonstrating its robustness.

5.3. Real-world Datasets

We evaluate on four real cryo-ET datasets: *G. hanseni* bio9-2, Vesicle, Escherichia phage T4, and Centriole. The *G. hanseni* bio9-2 dataset is a tilt series of 61 projections ranging from -60° to $+60^\circ$ at 2° intervals. Each tilt image measures 960×928 pixels with $5.41 \text{ \AA}/\text{pixel}$. The Vesicle dataset consists of 120 projections ranging from -59° to $+60^\circ$ at 1° intervals. Each tilt image measures 1024×1024 pixels with $8 \text{ \AA}/\text{pixel}$. The Escherichia phage T4 dataset contains 41 projections ranging from -60° to $+60^\circ$ at 3° intervals. Each tilt image measures 1024×1024 pixels with $1.558 \text{ \AA}/\text{pixel}$. The Centriole dataset is a tilt series of 64 projections ranging from -61.0° to $+65.0^\circ$ at 2° at intervals. Each tilt image measures 1024×1024 pixels with $10.1 \text{ \AA}/\text{pixel}$. The tomographic volumes for these specimens were reconstructed using the *tilt* program in IMOD [21].

5.4. Experiments on Real Cryo-ET data

Visual analysis. Figure 4 shows the visualized results of the real world cryo-ET datasets. From the results of *G.hanseni*, we can clearly see that the volume denoised by the our method are recovered with the best contrast. The phage structures in the Escherichia phage T4 can be eas-

ily identified without the darkness and edge blurriness after denoising, while others detailed structures remain blurred and dark. The datasets Vesicle and Centriole contain complex cellular structures which are difficult to denoise without abundant pre-defined knowledge. In such cases, our model can still derive denoised volumes with enough contrast, while preserving the ultrastructure integrity. The denoised volumes derived by the proposed model introduce fewer grid artifacts than the other results. Figure 5 presents $FSC_{e/o}^{-1}(0.5)$ curves for the *G.hanseni* and Phage, which illustrates that our method can perform better image restoration with higher self-consistency and introduce fewer false signal comparing with other methods.

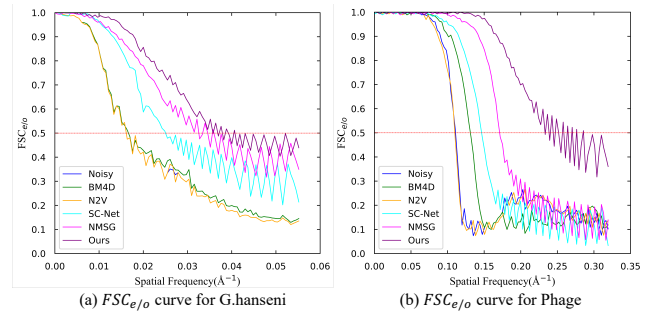


Figure 5. Examples of $FSC_{e/o}$ curves for the *G.hanseni* and Phage. Red dash line in the figures point out the position of $FSC_{e/o}=0.5$.

Quantitative analysis. As ground-truth is unavailable in real-world situations, we adopt a cross-validation metric

called $FSC_{e/o}$ [8] to assess the resolution of cryo-ET volumes. Table 4 shows the $FSC_{e/o}^{-1}(0.5)$ resolution calculated on the four real-world data. All the tomogram is calculated with subtomogram sized by $512^2 \times 100$. Results show that our method achieves the best resolution among other volumetric image denoising methods.

Table 4. Resolution estimated by $FSC_{e/o}^{-1}(0.5)$ (Angstrom, Å). For resolution of a tomogram, the lower is the better.

Dataset	G.hanseni	Vesicle	Phage	Centriole
Noisy	63.43	30.05	10.17	57.74
BM4D	61.08	29.44	9.30	57.37
N2V	63.41	30.01	10.15	57.65
SC-Net	40.22	22.67	6.93	38.21
NMSG	27.95	20.11	5.92	31.10
Ours	24.61	17.38	3.50	26.96

6. Ablation studies

Component analysis of loss function. To verify the effectiveness of our combined loss function, we conducted component analysis by systematically removing one or more components (\mathcal{L}_{guide} , \mathcal{L}_{edge} and \mathcal{L}_{TV}) and comparing the results with the full model. Table 5 indicates that removing any component significantly reduces performance, highlighting their importance in guiding the network to preserve contrast, edge, and texture information while regularizing the model. The full model produces the highest quality results (Figure 6), with better preservation of structural details and fewer artifacts. Thus, the combined loss function ensures balanced noise suppression and structural preservation, leading to high-quality denoised volumetric images.

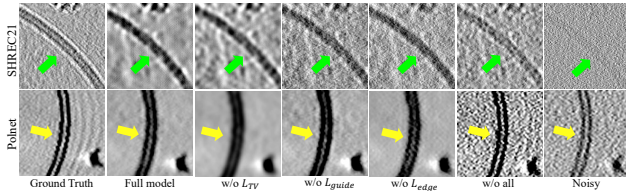


Figure 6. Visual results of component analysis on loss functions.

Table 5. PSNR/SSIM results for ablation study on the component analysis of the loss functions. (AWGN: $\sigma=0.2$).

Method	SHREC21	PolNet
Ours (w/o \mathcal{L}_{edge})	30.71 / 0.695	31.29 / 0.819
Ours (w/o \mathcal{L}_{guide})	35.93 / 0.644	33.24 / 0.875
Ours (w/o \mathcal{L}_{TV})	36.94 / 0.736	36.89 / 0.917
Ours (w/o all)	28.99 / 0.431	26.64 / 0.507
Ours (full model)	37.62 / 0.784	36.51 / 0.932

Study on noise patterns in simulated data. To rigorously assess the model’s robustness across various noise

conditions, we generated simulated tomograms using different noise patterns. Specifically, we introduced Gaussian noise ($\sigma=0.2$) to represent a common baseline scenario and Poisson noise ($\lambda=0.02$). We also included a mixture noise model with respective weights adjusted to ensure an overall noise level comparable to the individual noise types.

Table 6. Quantitative result of proposed methods under different noise patterns on simulated datasets. For each column, the **best** and **second-best** values are highlighted. (metrics: PSNR/SSIM)

Noise		Shrec2020	Shrec2021	PolNet
Gaussian ($\sigma = 0.2$)	noisy	18.12 / 0.377	18.34 / 0.142	21.17 / 0.344
	denoised	<u>35.79</u> / 0.936	37.64 / 0.784	36.51 / 0.932
Poisson ($\lambda=0.02$)	noisy	16.81 / 0.332	17.23 / 0.129	17.56 / 0.306
	denoised	31.57 / 0.873	31.49 / 0.695	<u>33.32</u> / <u>0.901</u>
Mixture (weights adjusted)	noisy	16.11 / 0.293	16.59 / 0.104	17.44 / 0.273
	denoised	25.96 / 0.522	24.81 / 0.371	26.42 / 0.686

Study on network components. The effect of the DCA module and volume unshuffle/shuffle (VU/S) is illustrated in Figure 7 and detailed in Table 7. In Table 7 (a), we adopt a standard 3-layer UNet. For Table 7 (b), we use max pooling for downsampling and bilinear interpolation for upsampling. For Table 7 (c), the D-BSN block replaces the DCA module. Overall, the combination of DCA and VU/S (Table 7 (d)) exhibits the best performance compared to other ablated results.

Table 7. Quantitative analysis of the effects of the DCA module and VU/S. (AWGN: $\sigma=0.10$, metrics: PSNR(db)/SSIM).

	DCA	VU/S	SHREC20	SHREC21
(a) UNet	-	-	25.62 / 0.593	24.33 / 0.249
(b) DCA+UNet	✓	-	26.25 / 0.607	23.93 / 0.255
(c) D-BSN+VU/S	-	✓	31.81 / 0.893	33.79 / 0.726
(d) DCA+VU/S	✓	✓	36.02 / 0.941	39.23 / 0.832

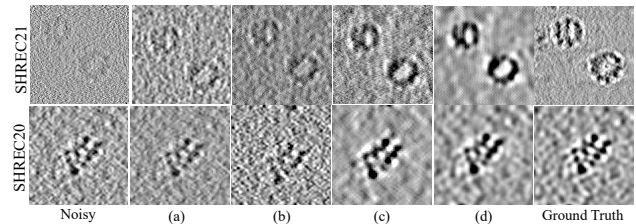


Figure 7. Visual results of study on volume unshuffle/shuffle.

7. Conclusions

This study presents a novel U-shape self-supervised learning model for denoising Cryo-ET volumetric images. By incorporating a \mathcal{J} -invariant BSN and volume-unshuffle/shuffle technique, our model demonstrates superior noise reduction and structural preservation compared to existing methods. The comprehensive results validate the effectiveness of our approach, offering a powerful tool for researchers in structural biology to achieve more accurate and detailed visualizations of cellular structures.

References

- [1] Marc Adrian, Jacques Dubochet, Jean Lepault, and Alasdair W McDowell. Cryo-electron microscopy of viruses. *Nature*, 308(5954):32–36, 1984. 1
- [2] Forest Agostinelli, Michael R Anderson, and Honglak Lee. Adaptive multi-column deep neural networks with application to robust image denoising. *Advances in neural information processing systems*, 26, 2013. 2
- [3] Jimmy Lei Ba, Jamie Ryan Kiros, and Geoffrey E Hinton. Layer normalization. *arXiv preprint arXiv:1607.06450*, 2016. 5
- [4] Joshua Batson and Loic Royer. Noise2self: Blind denoising by self-supervision. In *International Conference on Machine Learning*, pages 524–533. PMLR, 2019. 1, 3
- [5] Tristan Bepler, Kotaro Kelley, Alex J Noble, and Bonnie Berger. Topaz-denoise: general deep denoising models for cryoem and cryoet. *Nature communications*, 11(1):5208, 2020. 1, 2
- [6] Antoni Buades, Bartomeu Coll, and J-M Morel. A non-local algorithm for image denoising. In *2005 IEEE computer society conference on computer vision and pattern recognition (CVPR'05)*, volume 2, pages 60–65. Ieee, 2005. 1, 2, 6
- [7] Tim-Oliver Buchholz, Alexander Krull, Réza Shahidi, Gaia Pigino, Gáspár Jékely, and Florian Jug. Content-aware image restoration for electron microscopy. *Methods in cell biology*, 152:277–289, 2019. 2
- [8] Giovanni Cardone, Kay Grünewald, and Alasdair C Steven. A resolution criterion for electron tomography based on cross-validation. *Journal of structural biology*, 151(2):117–129, 2005. 8
- [9] Liangyu Chen, Xiaojie Chu, Xiangyu Zhang, and Jian Sun. Simple baselines for image restoration. In *European conference on computer vision*, pages 17–33. Springer, 2022. 2, 5
- [10] Sung-Jin Cho, Seo-Won Ji, Jun-Pyo Hong, Seung-Won Jung, and Sung-Jea Ko. Rethinking coarse-to-fine approach in single image deblurring. In *Proceedings of the IEEE/CVF international conference on computer vision*, pages 4641–4650, 2021. 2
- [11] P Kingma Diederik. Adam: A method for stochastic optimization. (*No Title*), 2014. 6
- [12] Weisheng Dong, Peiyao Wang, Wotao Yin, Guangming Shi, Fangfang Wu, and Xiaotong Lu. Denoising prior driven deep neural network for image restoration. *IEEE transactions on pattern analysis and machine intelligence*, 41(10):2305–2318, 2018. 2
- [13] Achilleas S Frangakis and Reiner Hegerl. Noise reduction in electron tomographic reconstructions using nonlinear anisotropic diffusion. *Journal of structural biology*, 135(3):239–250, 2001. 1, 2, 6
- [14] J Frank, BF McEwen, M Radermacher, JN Turner, and CL Rieder. Three-dimensional tomographic reconstruction in high voltage electron microscopy. *Journal of electron microscopy technique*, 6(2):193–205, 1987. 1
- [15] Joachim Frank, Michael Radermacher, Pawel Penczek, Jun Zhu, Yanhong Li, Mahieddine Ladjadj, and Ardean Leith. Spider and web: processing and visualization of images in 3d electron microscopy and related fields. *Journal of structural biology*, 116(1):190–199, 1996. 6
- [16] Ishaan Gulrajani, Faruk Ahmed, Martin Arjovsky, Vincent Dumoulin, and Aaron C Courville. Improved training of wasserstein gans. *Advances in neural information processing systems*, 30, 2017. 1
- [17] Kaiming He, Xiangyu Zhang, Shaoqing Ren, and Jian Sun. Deep residual learning for image recognition. In *Proceedings of the IEEE conference on computer vision and pattern recognition*, pages 770–778, 2016. 5
- [18] Phillip Isola, Jun-Yan Zhu, Tinghui Zhou, and Alexei A Efros. Image-to-image translation with conditional adversarial networks. In *Proceedings of the IEEE conference on computer vision and pattern recognition*, pages 1125–1134, 2017. 2
- [19] Viren Jain and Sebastian Seung. Natural image denoising with convolutional networks. *Advances in neural information processing systems*, 21, 2008. 1, 2
- [20] Hyemi Jang, Junsung Park, Dahuin Jung, Jaihyun Lew, Ho Bae, and Sungroh Yoon. Puca: patch-unshuffle and channel attention for enhanced self-supervised image denoising. *Advances in Neural Information Processing Systems*, 36, 2024. 3, 4
- [21] James R Kremer, David N Mastronarde, and J Richard McIntosh. Computer visualization of three-dimensional image data using imod. *Journal of structural biology*, 116(1):71–76, 1996. 7
- [22] Alexander Krull, Tim-Oliver Buchholz, and Florian Jug. Noise2void-learning denoising from single noisy images. In *Proceedings of the IEEE/CVF conference on computer vision and pattern recognition*, pages 2129–2137, 2019. 1, 3, 6
- [23] Samuli Laine, Tero Karras, Jaakko Lehtinen, and Timo Aila. High-quality self-supervised deep image denoising. *Advances in Neural Information Processing Systems*, 32, 2019. 3
- [24] Wooseok Lee, Sanghyun Son, and Kyoung Mu Lee. Apbsn: Self-supervised denoising for real-world images via asymmetric pd and blind-spot network. In *Proceedings of the IEEE/CVF Conference on Computer Vision and Pattern Recognition*, pages 17725–17734, 2022. 1, 2, 3
- [25] Jaakko Lehtinen, Jacob Munkberg, Jon Hasselgren, Samuli Laine, Tero Karras, Miika Aittala, and Timo Aila. Noise2noise: Learning image restoration without clean data. *arXiv preprint arXiv:1803.04189*, 2018. 2
- [26] Matteo Maggioni, Vladimir Katkovnik, Karen Egiazarian, and Alessandro Foi. Nonlocal transform-domain filter for volumetric data denoising and reconstruction. *IEEE transactions on image processing*, 22(1):119–133, 2012. 2, 6
- [27] Mauro Maiorca, Eric Hanssen, Edmund Kazmierczak, Bohumil Maco, Misha Kudryashev, Richard Hall, Harry Quiney, and Leann Tilley. Improving the quality of electron tomography image volumes using pre-reconstruction filtering. *Journal of structural biology*, 180(1):132–142, 2012. 2
- [28] Xiaojiao Mao, Chunhua Shen, and Yu-Bin Yang. Image restoration using very deep convolutional encoder-decoder

- networks with symmetric skip connections. *Advances in neural information processing systems*, 29, 2016. [2](#)
- [29] Antonio Martinez-Sanchez, Lorenz Lamm, Marion Jasnin, and Harold Phelippeau. Simulating the cellular context in synthetic datasets for cryo-electron tomography. *bioRxiv*, pages 2023–05, 2023. [6](#)
- [30] Fausto Milletari, Nassir Navab, and Seyed-Ahmad Ahmadi. V-net: Fully convolutional neural networks for volumetric medical image segmentation. In *2016 fourth international conference on 3D vision (3DV)*, pages 565–571. Ieee, 2016. [6](#)
- [31] Nick Moran, Dan Schmidt, Yu Zhong, and Patrick Coady. Noisier2noise: Learning to denoise from unpaired noisy data. In *Proceedings of the IEEE/CVF Conference on Computer Vision and Pattern Recognition*, pages 12064–12072, 2020. [2](#)
- [32] Beat Münch, Pavel Trtik, Federica Marone, and Marco Stamparoni. Stripe and ring artifact removal with combined wavelet—fourier filtering. *Optics express*, 17(10):8567–8591, 2009. [1](#)
- [33] Ren Ng. Fourier slice photography. In *ACM Siggraph 2005 Papers*, pages 735–744, 2005. [2](#)
- [34] Adam Paszke, Sam Gross, Francisco Massa, Adam Lerer, James Bradbury, Gregory Chanan, Trevor Killeen, Zeming Lin, Natalia Gimelshein, Luca Antiga, et al. Pytorch: An imperative style, high-performance deep learning library. *Advances in neural information processing systems*, 32, 2019. [6](#)
- [35] Olaf Ronneberger, Philipp Fischer, and Thomas Brox. U-net: Convolutional networks for biomedical image segmentation. In *Medical image computing and computer-assisted intervention—MICCAI 2015: 18th international conference, Munich, Germany, October 5-9, 2015, proceedings, part III 18*, pages 234–241. Springer, 2015. [4](#)
- [36] Carlo Tomasi and Roberto Manduchi. Bilateral filtering for gray and color images. In *Sixth international conference on computer vision (IEEE Cat. No. 98CH36271)*, pages 839–846. IEEE, 1998. [1](#), [2](#), [6](#)
- [37] Martin Turk and Wolfgang Baumeister. The promise and the challenges of cryo-electron tomography. *FEBS letters*, 594(20):3243–3261, 2020. [1](#)
- [38] Peter van der Heide, Xiao-Ping Xu, Brad J Marsh, Dorit Hanein, and Niels Volkman. Efficient automatic noise reduction of electron tomographic reconstructions based on iterative median filtering. *Journal of structural biology*, 158(2):196–204, 2007. [2](#)
- [39] Xiaohe Wu, Ming Liu, Yue Cao, Dongwei Ren, and Wangmeng Zuo. Unpaired learning of deep image denoising. In *European conference on computer vision*, pages 352–368. Springer, 2020. [2](#), [3](#), [5](#)
- [40] Junyuan Xie, Linli Xu, and Enhong Chen. Image denoising and inpainting with deep neural networks. *Advances in neural information processing systems*, 25, 2012. [1](#), [2](#)
- [41] Zhidong Yang, Dawei Zang, Hongjia Li, Zhao Zhang, Fa Zhang, and Renmin Han. Self-supervised noise modeling and sparsity guided electron tomography volumetric image denoising. *Ultramicroscopy*, 255:113860, 2024. [2](#), [6](#)
- [42] Zhidong Yang, Fa Zhang, and Renmin Han. Self-supervised cryo-electron tomography volumetric image restoration from single noisy volume with sparsity constraint. In *Proceedings of the IEEE/CVF International Conference on Computer Vision*, pages 4056–4065, 2021. [1](#), [3](#), [6](#)
- [43] Zongsheng Yue, Qian Zhao, Lei Zhang, and Deyu Meng. Dual adversarial network: Toward real-world noise removal and noise generation. In *Computer Vision—ECCV 2020: 16th European Conference, Glasgow, UK, August 23–28, 2020, Proceedings, Part X 16*, pages 41–58. Springer, 2020. [2](#)
- [44] Syed Waqas Zamir, Aditya Arora, Salman Khan, Munawar Hayat, Fahad Shahbaz Khan, and Ming-Hsuan Yang. Restormer: Efficient transformer for high-resolution image restoration. In *Proceedings of the IEEE/CVF conference on computer vision and pattern recognition*, pages 5728–5739, 2022. [5](#)
- [45] Syed Waqas Zamir, Aditya Arora, Salman Khan, Munawar Hayat, Fahad Shahbaz Khan, Ming-Hsuan Yang, and Ling Shao. Multi-stage progressive image restoration. In *Proceedings of the IEEE/CVF conference on computer vision and pattern recognition*, pages 14821–14831, 2021. [2](#)
- [46] Dan Zhang, Fangfang Zhou, Yuwen Jiang, and Zhengming Fu. Mm-bsn: Self-supervised image denoising for real-world with multi-mask based on blind-spot network. In *Proceedings of the IEEE/CVF Conference on Computer Vision and Pattern Recognition*, pages 4188–4197, 2023. [1](#), [2](#), [3](#)
- [47] Dan Zhang, Fangfang Zhou, Yuanzhou Wei, Xiao Yang, and Yuan Gu. Unleashing the power of self-supervised image denoising: A comprehensive review. *arXiv preprint arXiv:2308.00247*, 2023. [2](#)
- [48] Kai Zhang, Wangmeng Zuo, Yunjin Chen, Deyu Meng, and Lei Zhang. Beyond a gaussian denoiser: Residual learning of deep cnn for image denoising. *IEEE transactions on image processing*, 26(7):3142–3155, 2017. [1](#), [2](#), [6](#)
- [49] Kai Zhang, Wangmeng Zuo, and Lei Zhang. Ffdnet: Toward a fast and flexible solution for cnn-based image denoising. *IEEE Transactions on Image Processing*, 27(9):4608–4622, 2018. [2](#), [6](#)